



## Heat wave contribution to 2022's extreme glacier melt from automated real-time ice ablation readings

Aaron Cremona<sup>1,2</sup>, Matthias Huss<sup>1,2,3</sup>, Johannes Marian Landmann<sup>1,2,4</sup>, Joël Borner<sup>1,5</sup>, and Daniel Farinotti<sup>1,2</sup>

<sup>1</sup>Laboratory of Hydraulics, Hydrology and Glaciology (VAW), ETH Zurich, Zurich, Switzerland

<sup>2</sup>Swiss Federal Institute for Forest, Snow and Landscape Research (WSL), Birmensdorf, Switzerland

<sup>3</sup>Department of Geosciences, University of Fribourg, Fribourg, Switzerland

<sup>4</sup>Federal Office of Meteorology and Climatology, MeteoSwiss, Zurich-Airport, Switzerland

<sup>5</sup>WSL Institute for Snow and Avalanche Research SLF, Davos, Switzerland

**Correspondence:** Aaron Cremona ([cremona@vaw.baug.ethz.ch](mailto:cremona@vaw.baug.ethz.ch))

**Abstract.** Accelerating glacier melt rates were observed during the last decades. Substantial ice loss occurs particularly during heat waves that are expected to intensify in the future. Because measuring and modelling glacier mass balance at the daily scale remains challenging, short-term mass balance variations, including extreme melt events, are poorly captured. Here, we present a novel approach based on computer-vision techniques for automatically determining daily mass balance variations at the local scale. The approach is based on the automated recognition of color-taped ablation stakes from camera images, and is tested and validated at six stations installed on three Alpine glaciers during the summers of 2019-2022. Our approach produces daily mass balance with an uncertainty of  $\pm 0.81 \text{ cm w.e. d}^{-1}$ , which is about half of the accuracy obtained from manual read outs. The automatically retrieved daily mass balances at the six sites were compared to average daily mass balances over the last decade derived from seasonal in situ observations to detect and assess extreme melt events. This allows analyzing the impact that the summer heat waves which occurred in 2022 had on glacier melt. Our results indicate 23 days with extreme melt, showing a strong correspondence between the heat wave periods and extreme melt events. The combination of below-average winter snow fall and a suite of summer heat waves led to unprecedented glacier mass loss. The Swiss-wide glacier storage change during the 25 days of heat waves in 2022 is estimated as  $1.27 \pm 0.10 \text{ km}^3$  of water, corresponding to 35% of the overall glacier mass loss during that summer. Compared to the average course of the past decade, the 25 days of heat waves in 2022 caused a glacier mass loss that corresponds to 56% of the overall mass loss experienced on average during summers 2010-2020, demonstrating the relevance of heat waves for seasonal melt.



## 1 Introduction

The prominent and accelerating shrinkage of glaciers worldwide driven by climate change is widely documented (Church et al., 2001; Zemp et al., 2019; Hugonnet et al., 2021). The projected glacier loss will impact sea-level rise (Parkes and Marzeion, 2018; Marzeion et al., 2020), water resources (Immerzeel et al., 2020), and cryosphere-related hazards (Stoffel and Huggel, 2012). In the Alps, the substantial losses with glacier mass balances of about  $-1 \text{ m.w.e. a}^{-1}$  (Huss, 2012; Davaze et al., 2020) have a significant influence on the runoff regime (Farinotti et al., 2016; Huss and Hock, 2018), thus impacting water supply (Immerzeel et al., 2010) and hydropower production (Patro et al., 2018; Schaeffli et al., 2019)). Glacier mass balance directly reflects fluctuations in climatic forcing (Ohmura et al., 2007), drives ice dynamics, and determines runoff generation, making it a primary indicator for glacier and climate monitoring (Zemp et al., 2015; Trewin et al., 2021). Despite glacier mass balance has been studied extensively with remote sensing (Bamber and Rivera, 2007), in-situ observations (Zemp et al., 2009), and modelling approaches (Hock, 2005; Hock et al., 2019), daily-scale mass balance variations remain mostly unexplored.

Glacier mass balance at the scale of entire glaciers and mountain ranges is often derived from remote sensing products via the geodetic method (Dussaillant et al., 2018; Denzinger et al., 2021; Hugonnet et al., 2021). In it, ice volume change is obtained by differentiating two digital elevation models (DEMs) and translated to mass change by assuming a given density for the volume change (Huss, 2013). However, there are some requirements to be met when calculating the geodetic mass balance, one of these being that the two DEMs should be several years apart (Huss, 2013). Hence, this method is not suitable to assess short-term mass balance variations.

Glacier-wide seasonal and annual mass balances are routinely computed from point measurements (Ostrem and Stanley, 1969; Zemp et al., 2009, 2013; Carturan et al., 2016; Sold et al., 2016; O'Neel et al., 2019). The direct glaciological method allows for deriving accumulation and ablation components with ablation stakes, snow probes, and snow pits distributed over the glacier (Ostrem and Stanley, 1969; Dyurgerov et al., 2002; Geibel et al., 2022). Glacier-wide mass balance is then calculated by interpolating the point balances of the network over the entire surface. Methods to do so range from a simple elevation dependence, over hand-drawn contours of equal mass balance, to more advanced statistical methods such as kriging and distributed modelling constrained with local measurements (Dyurgerov et al., 2002; Cogley et al., 2010). Even though glacier-wide mass balance is not directly measured, it is able to capture the temporal variability of glacier mass balance (Fountain and Vecchia, 1999; Thibert et al., 2018). Several studies investigated the temporal variability of mass balance on seasonal to monthly basis, relying on both measurements and modeling (Braithwaite, 1995; Pellicciotti et al., 2005; Huss and Bauder, 2009; Azam et al., 2014; Sold et al., 2016; Mölg et al., 2017). However, models are calibrated on observations, therefore the temporal resolution of these approaches is often limited by the low frequency of measurements.

Recently, techniques to measure mass balance at higher temporal resolution have emerged. Automatic weather station were employed to measure the components of the energy budget and, thus, model the glacier surface energy balance at sub-daily resolution (Cullen et al., 2007; Fitzpatrick et al., 2017). Gugerli et al. (2019) presented a method for continuous snow water equivalent observations on a glacier surface during winter, relying on a cosmic ray sensor. Automated ablation stakes were developed too. A2PS contributors (2021) presented a station deployed on the glacier surface with a steel wire anchored sev-



eral meter below the ice surface. As the surface melts, the station lowers, the wire is coiled by the station, and the vertical displacement is derived. A different approach was implemented by Landmann et al. (2021) who installed automated cameras monitoring color-coded ablation stakes with a temporal resolution of 20 minutes. From the image time series, the daily melt was derived.

Because these novel methods allows measuring mass balance at high temporal resolution, they provide new observation-based insights into short-term mass balance variations, including extreme melt events. In this study, we present an approach for the automated reading of the color-coded ablation stakes proposed by Landmann et al. (2021), which allows deriving daily point mass balances via the direct glaciological method. We developed an algorithm that takes an image time series depicting the stake during the season, acquired at 20-minute intervals, and provides the daily surface mass balances. The method is tested during the summers of 2019-2021 for six stations installed on three Swiss glaciers. The performance of the algorithm is validated against (i) visual readings of the image time series, and (ii) in-situ measurements. Automatically-derived daily mass balances at the six sites are compared with average daily mass balances over the last decade derived from seasonal in situ observations and modelling to detect and assess extreme melt events. Extreme melt events that occurred during the summer of 2022 are investigated in more detail to evaluate the significance of heat waves for seasonal ice ablation and water runoff. Finally, we discuss the suitability of the method for the detection of extreme glacier melt events at the scale of the Swiss Alps based on point measurements.

## 2 Study site and field data

The three test sites, i.e. Findelgletscher, Glacier de la Plaine Morte, and Rhonegletscher, are medium-sized to large Alpine glaciers located in the central and in the southwestern part of Switzerland (Fig. 1, Table 1). The three glaciers are part of the long-term monitoring program GLAMOS (Glacier Monitoring Switzerland). The seasonal and annual mass balances are derived via the glaciological method, exploiting a network of 5 to 12 ablation stakes distributed over the glaciers' entire elevation range. In 2019, six autonomous stations equipped with a camera observing an ablation stake were installed on these glaciers in order to monitor local mass balance at a daily basis: FIN 1 (2551 m.a.s.l.) and FIN 2 (3015 m.a.s.l.) on Findelgletscher, PLM (2689 m.a.s.l.) on Glacier de la Plaine Morte, and RHO 1 (2241 m.a.s.l.), RHO 2 (2392 m.a.s.l.) and RHO 3 (2589 m.a.s.l.) on Rhonegletscher (Fig. 1, Table 1). The station setup consists of a camera and an aluminium stake that is marked with tapes

**Table 1.** Glacier and station characteristics. Area and elevation refer to the year 2019 (GLAMOS, 2021).

	Area (km <sup>2</sup> )	Elevation range (m a.s.l.)	Camera stations
Findelgletscher	12.7	2561-3937	FIN 1 (2551 m a.s.l.) FIN 2 (3015 m a.s.l.)
Plaine Morte	7.1	2470-2828	PLM (2689 m a.s.l.)
Rhonegletscher	15.3	2223-3596	RHO 1 (2241 m a.s.l.) RHO 2 (2392 m a.s.l.) RHO 3 (2589 m a.s.l.)

of different colors, placed at 2-centimeter intervals (Fig. 2). The only static element of the system is the stake, which is drilled into the ice. The camera construction, instead, is placed at the glacier surface and slides along the fixed stake. The station setup

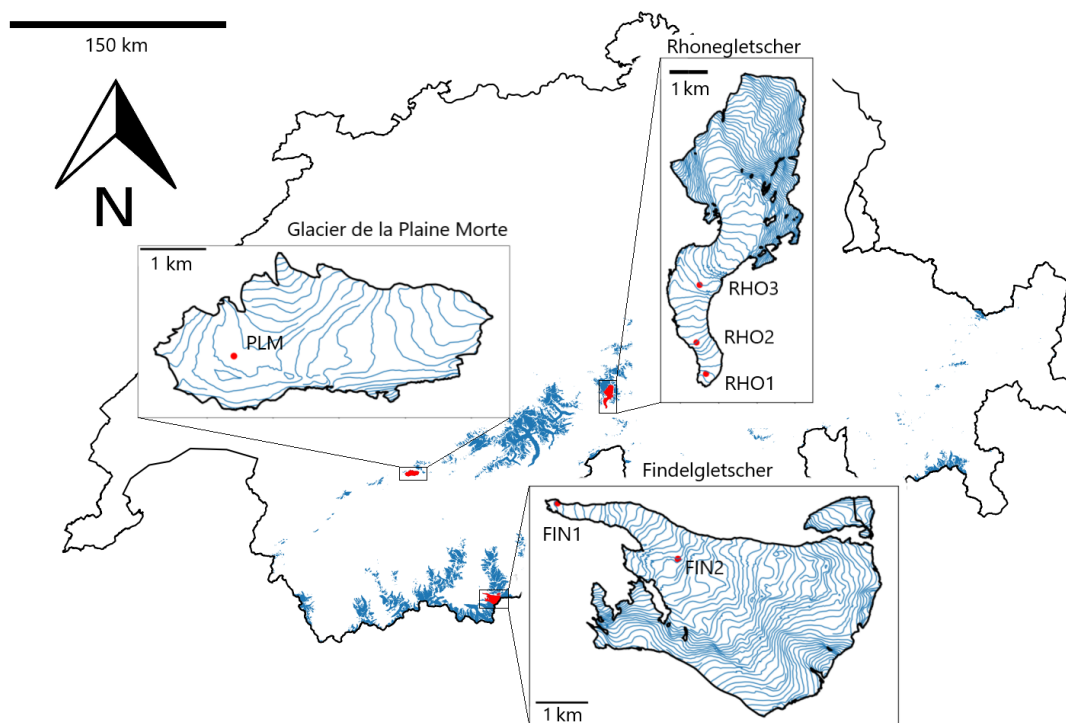


**Figure 1.** Study site overview. The locations of the six stations installed on Glacier de la Plaine Morte (station PLM), Rhonegletscher (stations RHO 1, RHO 2, and RHO 3), and Findelgletscher (stations FIN 1 and FIN 2) are indicated. Glacier outlines refer to the Swiss Glacier Inventory 2016 (Linsbauer et al., 2021), whereas region boundaries and contour lines are provided by swisstopo.

thus uses the camera as a reference point. When observing the images acquired every 20 minutes during the ablation period, it thus appears that the stake is emerging from the ice. To automatically read the stake, a computer-vision algorithm is used to derive the stake displacement between two images. From this, the mass balance is derived. The six stations were operated during the summer seasons of 2019-2022 (see Table 2 for the individual operation periods), providing point mass balances at the daily time scale.

**Table 2.** Operation periods of all stations during the summer seasons 2019-2021.

Year	FIN 2	FIN 1	PLM	RHO 3	RHO 2	RHO 1
2019	27.06-17.09	27.06-17.09	19.06-19.09	26.07-03.10	13.08-03.10	26.07-03.10
2020	16.06-15.09	16.06-15.09	30.06-04.09	24.04-24.09	15.06-24.09	15.06-24.09
2021	08.04-22.09	08.04-22.09	26.06-18.09	21.04-29.09	21.04-29.09	28.06-29.09
2022	not installed	06.04-05.09	04.04-23.09	21.04-24.09	not installed	not installed

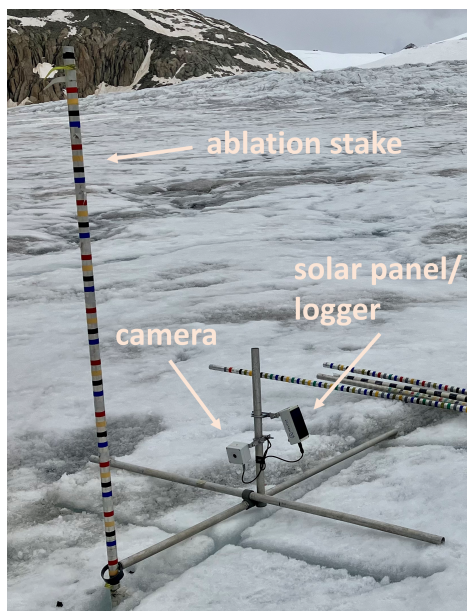


**Figure 2.** The station setup used to monitor the daily mass balance. The camera acquires pictures of the taped ablation stake every 20 minutes. For details of the setup, refer to Landmann et al. (2021).

### 3 Methods

#### 85 3.1 Automated stake reading

We develop an algorithm that exploits computer-vision techniques to automatically derive point mass balance series from a sequence of close-range images of an ablation stake acquired during the melting season. The basis for our algorithm is provided by OpenCV, an open-source library that includes several functions designed to process images and videos (Bradski, 2000). In particular, the framework is built on `matchTemplate`, a function able to detect objects in an image based on a template of the object to be identified (OpenCV, 2022). The function iteratively compares the template with every portion of the target image, and the correlation between every image portion and the template is returned. A low correlation indicates that the image portion differs significantly from the template, whereas the higher the correlation, the more similar the two images are. A correlation of 1 indicates perfect agreement and can only be obtained if the template is part of the target image. The `matchTemplate` function may be employed in two different ways: 1) to detect a single object, and 2) to detect multiple objects. In the first case, the object is detected by simply selecting the pixel with the maximum correlation value. In the second case, every pixel with a correlation above a certain threshold is depicted as a match.

For our application, we want to detect the largest number of tapes that are placed on the stake in every image. Since a tape may look different in two subsequent images (e.g. because of changes in the illumination, caused by different cloud conditions),



100 a relatively low correlation threshold of 0.75 is chosen. The stability of the method is also affected by the choice of template, and a tape stripe with high saturation and favourable illumination has to be preferred.

The choice of a low correlation threshold has also some drawbacks. In particular, this can cause other features in the images to be wrongly detected as tapes (Fig. 3). A two-step filtering procedure is therefore applied. The first step consists of removing duplicate matches to avoid redundancy. Such duplicate matches stem from the fact that matchTemplate operates pixelwise, and that many matches are found in the proximity of a tape. Clusters of matches are reduced to single matches according to the  
105 highest correlation within the cluster (Fig. 3). The second step consists of a collinearity check. Because all tapes are placed on the stake, i.e. on a linear feature, the correct matches are collinear. Here, we assume that the line intersecting the highest number of matches corresponds to the stake. Matches that do not intersect this line are probably located off the stake, and correspond to features that are wrongly detected and thus filtered out. After this procedure, only collinear and non-redundant matches are preserved, corresponding to the tapes placed on the ablation stake.

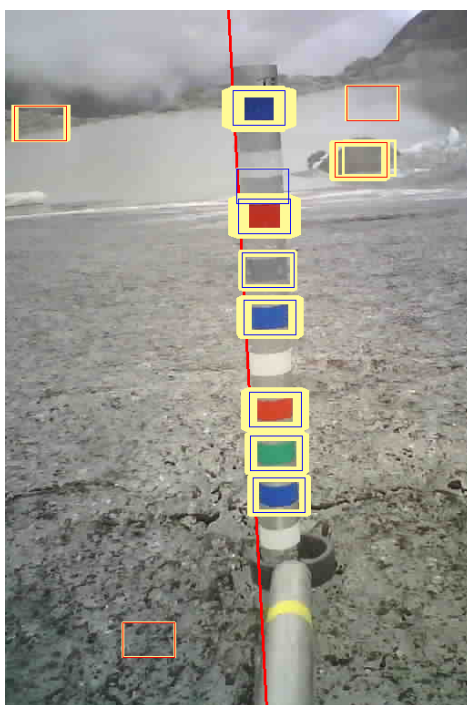


**Figure 3.** Two-step filtering procedure. (1) Clusters of matches (yellow) are reduced to single matches (red). (2) Non-collinear matches, i.e. not intersecting the red, almost-vertical line, are filtered out. Tapes that are located on the stake are preserved (blue).

110 An important limitation of matchTemplate is that it is unknown which match in a given image corresponds to which one in the subsequent image. However, most of the superimposed matches that are detected in two consecutive frames (Fig. 4 d) experience a very similar displacement. This is because the tapes lie on the stake, and thus move together, meaning that the displacement must be the same for every tape. Exploiting this property, the difference in position for all possible tape



combinations is calculated, and projected onto the stake axis with the following equation:

$$115 \quad d_k = \frac{y_{p,i-1} - y_{q,i}}{\cos \alpha_i}. \quad (1)$$

Here,  $\alpha$  is the stake inclination with respect to the vertical axis,  $y$  is the coordinate of a match in the current ( $i$ ) or previous ( $i - 1$ ) image,  $q \in [0, m]$  is the number of matches in image  $i$ ,  $p \in [0, n]$  is the number of matches in image  $i - 1$ , and  $d_k$  is the displacement between two matches in two consecutive images projected to the stake axis ( $k \in [0, (m \cdot n)]$ ). Finally, the displacement occurring most frequently is taken as the stake displacement.

120 Figure 4 shows this procedure with an example: in Figure 4 a, ten tapes are detected (highlighted in blue), whereas in Figure 4 b, which is the subsequent camera image, twelve tapes are detected (highlighted in yellow). By calculating the difference of the position between all combinations of tapes, the most frequent displacement, occurring eight times, corresponds to 0.668 pixels (Fig. 4 d). This is taken as stake displacement during the considered time period, and thus, as vertical ice melt. The procedure works recursively, meaning that if the stake displacement between the current image (index  $i$ ) and the previous

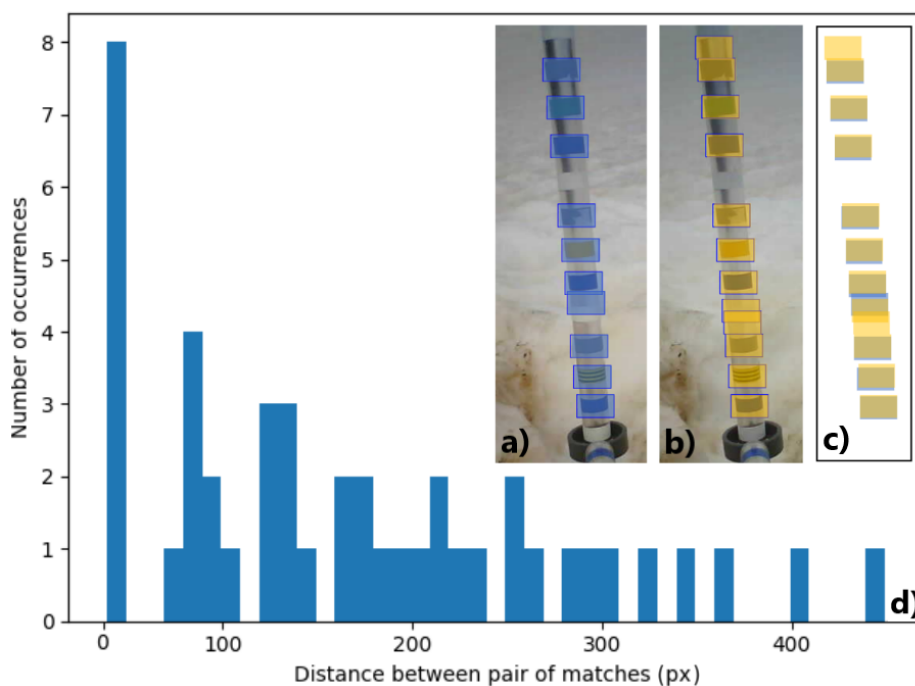


**Figure 4.** Stake displacement calculation. (a) Filtered matches in image  $i-1$  in blue. (b) Filtered matches in image  $i$  in yellow. (c) The two sets of matches are superimposed. (d) Occurrence of displacements  $d_k$  resulting from the difference of the positions between all possible combinations of tapes. The most frequent displacement in this case corresponds to 0.668 pixels, which is taken as stake displacement.

125 image (index  $i-1$ ) cannot be calculated, then images  $i$  and  $i-2$  are compared. This can generally be repeated up to 20 times, afterwards which the correlation becomes too low to calculate any displacement.



Pixel displacements can be transformed into metric units by multiplying them with a conversion factor  $c$  according the following equation:

$$c = \frac{d_{\text{ref,cm}}}{d_{\text{ref,px}}} \tag{2}$$

130 Here,  $d_{\text{ref,px}}$  is the most frequent distance between all possible tape combinations in an image, and  $d_{\text{ref,cm}} = 4 \text{ cm}$  is the reference distance between two tapes. In the example of Figure 4 a, the average distance between the tapes corresponds to 42.7 px, resulting in a conversion factor of  $c = 0.094 \text{ cm px}^{-1}$ . This conversion method has the advantage of compensating for distortion errors. In fact, depending on the relative angle between the camera and the stake, the measured distance between two tapes at the top of the stake can differ considerably from the distance between two tapes at the bottom of the stake. The impact  
135 of such differences is reduced by taking the average pixel distance. Converting the displacements from pixel to metric units is the last step of the algorithm to derive the stake displacements, which is then converted to mass balance with a multiplication with the density of the surface material. For bare ice, a density of  $900 \text{ kg m}^{-3}$  is assumed. For snow-covered surfaces, a density of  $600 \text{ kg m}^{-3}$  is assumed, which is derived from two snow-density measurements conducted on Glacier de la Plaine Morte in June 2019 and 2020, thus accounting for similar snow conditions, i.e. a snowpack during summer ablation (Gugerli et al.,  
140 2019). During summer snowfall, the algorithm is not able to capture accumulation, and the stake displacement, equal to zero, is assumed as the ablation.

### 3.2 Validation of automated stake reading

The automated stake reading algorithm is tested and validated with the images from the six stations acquired in the summer seasons of 2019-2021. In some cases, we observed a deterioration of the tapes over time. This causes the algorithm to struggle  
145 because of lower correlations and the correlation threshold had to be manually adjusted for the algorithm to work properly (Table 3). For some stake segments with strongly deteriorated tapes, the algorithm was unable to process the entire image time series and stopped along the way. In these cases, i.e. 15% of the readings, the gap was filled with visual readings.

**Table 3.** Correlation threshold used to process the image time series during the seasons 2019-2022. Stations FIN 2, RHO 2, and RHO 1 were not operated during the summer 2022 and thresholds are therefore not given. For PLM in 2022, the strong degradation of the tapes only enabled visual readings (as opposed to automated ones).

	FIN 2	FIN 1	PLM	RHO 3	RHO 2	RHO 1
2019	0.75	0.75	0.75	0.75	0.75	0.75
2020	0.70	0.75	0.67	0.70	0.75	0.75
2021	0.75	0.70	0.70	0.70	0.70	0.70
2022	-	0.69	-	0.72	-	-

For validation, the results of the automated algorithm were compared to (i) visual readings of the same image time series, and (ii) in-situ stake readings. Visual readings of the images are performed following Landmann et al. (2021). In-situ stake





150 readings were conducted two to five times per season in conjunction with the installation and maintenance of the stations, as well as with other field campaigns. By comparing the algorithms outcomes with the visual image readings, the daily errors of the automated approach can be computed. By comparing the algorithms' outcomes with the in-situ observations, the seasonal mean-absolute deviation (MAD) is derived. The results of this validation are provided in Sect. 4.1.

### 3.3 Mass balance anomalies and extreme events

155 The automated method provides point mass balance time series for the six stations. However, the stations are located on different glaciers and at various elevations implying that the time series cannot be directly compared against each other. In order to detect extreme melt events at a larger spatial scale, which is our target, we therefore aim at eliminating the local influences and at extracting a daily anomaly in the melt rates. This anomaly is computed with respect to an average course of the daily mass balance, where the average course refers to a longer temporal baseline. To obtain this, we rely on a combination of (i)  
160 local, seasonal mass balance measurements performed in the frame of GLAMOS at, or very close to, all six sites since at least 2010, and (ii) simple mass balance modelling for the period 2010-2020. More specifically, a daily, point-based accumulation and temperature-index melt model (Huss and Bauder, 2009; Huss et al., 2021) driven by nearby meteorological measurements is set up, and constrained in every year to exactly match the observed mass balance at both the date of the April and the September survey. This means that the seasonal mass balance variations are directly provided by the direct measurements,  
165 while the daily variations in between the surveys are given by the mass balance model.

Although the stations' locations are very close to the GLAMOS stakes (for which the long-term average mass balance is available), potential biases need to be corrected for. To correct for these potential biases, the average daily mass balance derived from the GLAMOS stakes during the summer period is adjusted to match the result derived for the automated reading of the camera observations during the respective years (Fig. 5). For example: for the hydrological year 2021 and station RHO 1,  
170 summer melt rates based on automated readings are slightly more negative than the ones inferred from combining the seasonal observations at the nearby reference stake and the modelling (Fig. 5 a). To correct for this bias, the daily difference is computed and superimposed on the long-term average daily mass balance curve as follows (see Fig. 5 b for illustration):

$$\dot{b}_{i,j,\text{GLAMOS,corr}} = \dot{b}_{i,j,\text{GLAMOS}} + (\overline{\dot{b}_{j,\text{cam}}} - \overline{\dot{b}_{j,\text{GLAMOS}}}). \quad (3)$$

Here,  $\dot{b}_{i,j,\text{GLAMOS}}$  is the melt rate at day  $i$  of year  $j$  that is derived from GLAMOS' seasonal measurements,  $\overline{\dot{b}_{j,\text{cam}}}$  is the  
175 average daily melt rate over the summer of year  $j$  that is derived from the camera observations, and  $\overline{\dot{b}_{j,\text{GLAMOS}}}$  is the average of  $\dot{b}_{i,j,\text{GLAMOS}}$  over the summer of year  $j$ .

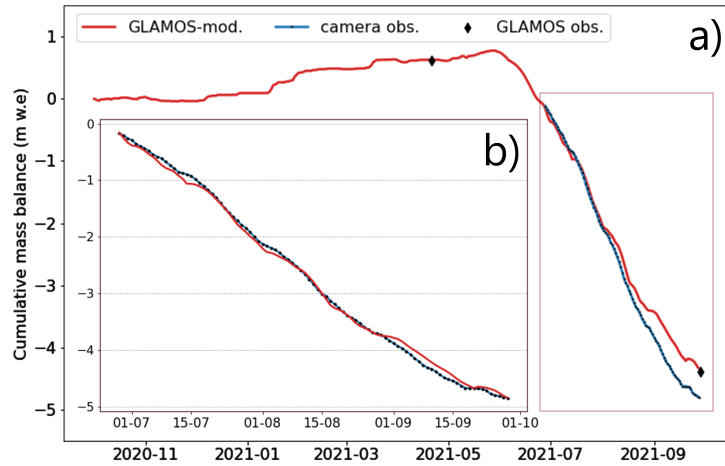


**Figure 5.** Bias correction for matching the long-term average daily mass balance to the automatically extracted daily ablation. a) Cumulative long-term average daily mass balance based on seasonal observations (black diamonds) combined with modelling (red) and observed daily mass balance at the station (blue). The example refers to RHO 1 during the period 01.10.2020-01.10.2021. Note that the observed daily mass balance is only available during the summer season. (b) Bias-corrected modelled and observed daily mass balances during the period 29.06-29.09.2021.

For each of the four years with camera observations, i.e. 2019-2022, we calculate the average daily difference between the melt rates derived from camera observations and the melt rates derived from seasonal measurements of GLAMOS (Eq. (4)):

$$\Delta \dot{b}_j = \overline{\dot{b}_{j,\text{cam}}} - \overline{\dot{b}_{j,\text{GLAMOS}}} \quad (4)$$

180 This yields four bias values  $\Delta \dot{b}_j$ , i.e. one value per year, that are averaged and superimposed on the long-term average daily mass balance (Eq. (5)):

$$\overline{\dot{b}_{i,2010-2020,\text{GLAMOS,corr}}} = \overline{\dot{b}_{i,2010-2020,\text{GLAMOS}}} + \overline{\Delta \dot{b}_j} \quad (5)$$

This procedure ensures correction of the biases resulting from location differences between the stakes of GLAMOS and those used for the automated mass balance reading.

185 To compare the mass balance signals across the different stations, the daily mass balance anomaly  $\Delta \dot{b}_{i,j}$  is calculated for each station (Eq. (6)):

$$\Delta \dot{b}_{i,j} = \dot{b}_{i,j,\text{cam}} - \overline{\dot{b}_{i,2010-2020,\text{GLAMOS,corr}}} \quad (6)$$

The mass balance anomaly is directly comparable across stations, and can be used to define an extreme melt event, i.e. an event in which the anomaly exceeds a certain threshold for all stations. We set this threshold to the 85% quantile of the negative anomalies observed during the years 2019-2021. The year 2022 was omitted when defining the threshold because of  
190 the extreme melt rates that do not represent the normal conditions. Although in statistical analysis the 97.5% or the 99.5%



quantiles are often chosen to define extreme events (Friederichs, 2010; Friederichs et al., 2018), we chose the 85% quantile because we aim at detecting prolonged periods with high melt rates, rather than only a few isolated days with maximal melt. The 85% quantile corresponds to  $-2.55 \text{ cm w.e d}^{-1}$ , and when this threshold is exceeded, the event is classified as extreme.

195 Note that this information at the point scale does not directly allow investigation of the influence of the heat waves on glacier melt at the regional scale, and upscaling is therefore needed.

### 3.4 Upscaling to regional mass balance

To derive the regional, i.e. Swiss-wide, daily glacier mass balance over summer of 2022, we combine the information at the point scale, i.e. the mass balance anomalies derived from the different stations, with information about the regional mass balance. We rely on data sets of glacier-wide seasonal mass balance for 20 glaciers (GLAMOS, 2021), a daily distributed mass balance model for these glaciers (Huss et al., 2021), and multi-decadal ice volume change (Fischer et al., 2015), as well as repeated inventories of surfaces areas for all glaciers (Linsbauer et al., 2021). First, glacier-specific anomalies in glacier-wide mass balance relative to the reference period 2010-2020 are extrapolated to all unmeasured glaciers based on inverse-distance weighting, including a higher weight for observations on the same side of the main Alpine weather divide (North/South). These anomalies are then superimposed on long-term average mass change rates available for every Swiss glacier from Fischer et al. (2015). This yields a series of annual glacier volume and mass changes at the scale of the Swiss Alps (see also Grab et al., 2021). Furthermore, daily time series of glacier-wide mass balance are available for the 20 glaciers with detailed measurements based on a combination of seasonal observations with a distributed mass balance model (Huss et al., 2021; GLAMOS, 2021). We attribute modelled daily mass balance of the closest series to every glacier of the most recent Swiss glacier inventory (Linsbauer et al., 2021) and match the daily time series to the glacier-specific annual mass balance (see above) by equally attributing the misfit to all days of the summer season (June-August). Overall, this procedure provides the average daily course of glacier mass balance as a mean over the period 2010-2020 for every single glacier.

205

210

To calculate the regional-scale mass balance for the summer of 2022, we combine the average regional mass balance 2010-2020 with the mean point mass balance anomaly calculated from the three stations operative in 2022 (Eq. (7)).

$$215 \quad \dot{B}_{i,2022} = \overline{\dot{B}_{i,2010-2020}} + \Delta \dot{b}_{i,2022}, \quad (7)$$

where  $i$  is day of the year,  $\dot{B}_{i,2022}$  is the computed regional mass balance for day  $i$  of 2022,  $\overline{\dot{B}_{i,2010-2020}}$  is the average regional mass balance of period 2010-2020 for day  $i$ , and  $\Delta \dot{b}_{i,2022}$  is the mean point mass balance anomaly for day  $i$  derived from the three stations providing daily measurements. This procedure allows the Swiss-wide glacier mass balance over the summer of 2022 to be estimated at the daily scale. Finally, we compute the Swiss-wide glacier storage change, which accounts for water that is produced from snow- and ice-melt on glacier surfaces over the melt season. The glacier storage change is computed by multiplying the Swiss-wide glacier mass balance with the glacierized area in Switzerland according to the last inventory (2016, Linsbauer et al., 2021).

220

## 4 Results

### 4.1 Performance of the automated algorithm

225 The cumulative mass balance obtained from the automated readings is very consistent with the manual readings and the in-situ  
observations (see example of station RHO 1 in Fig. 6 a-c). The good performance of the algorithm is proven by the boxplots  
showing the distribution of the daily deviations from the visual readings (Fig. 6 d-f). In 2019, the median daily deviation is  
0.06 cm and the mean deviation is  $-0.01$  cm (Fig. 6 d), in 2020, the values are  $-0.04$  cm and  $-0.11$  cm, respectively, and in  
2021, they are  $-0.33$  cm and  $-0.35$  cm, respectively (Fig. 6 f). The larger deviations in 2021 are likely a consequence of the  
230 tape degradation over time, which causes the tapes to loose color and to partially detach from the stake. Of note is the fact that  
the daily deviations are mostly negative, which might suggest that the automated algorithm overestimate melt when compared  
to the visual readings. However, the comparison of the automatically-retrieved cumulative mass balances with the reference  
mass balance (e.g. visual readings and in-situ observations) for all the six sites shows that the algorithm does not overestimate  
melt systematically (Fig. 7). With a mean-absolute deviation for the cumulative seasonal melt of 16 cm, Figure 7 shows a good  
235 correspondence of the automatically-retrieved mass balances with both the visual readings and in-situ observations.

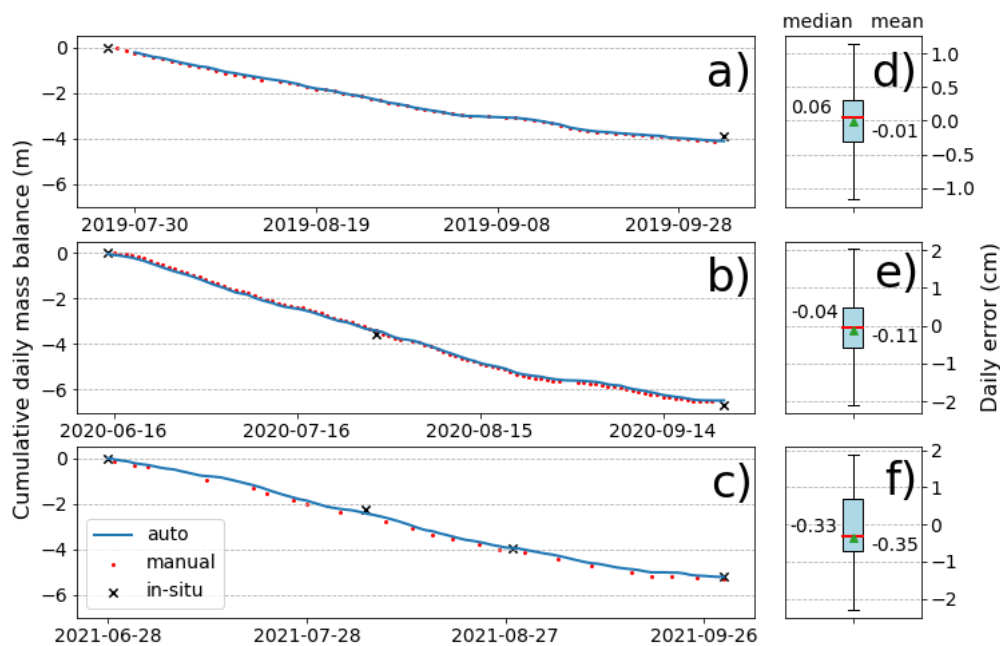


**Figure 6.** Validation of the automated mass balance readings for the station RHO 1. The cumulative daily mass balance for the years 2019 (a), 2020 (b), and 2021 (c) is shown. The mass balance from the automated method (blue) is validated against visual readings of the images (red) and in-situ observations (black). Panels (d-f) show daily deviations with respect to the visual readings over the seasons 2019, 2020, and 2021, respectively.

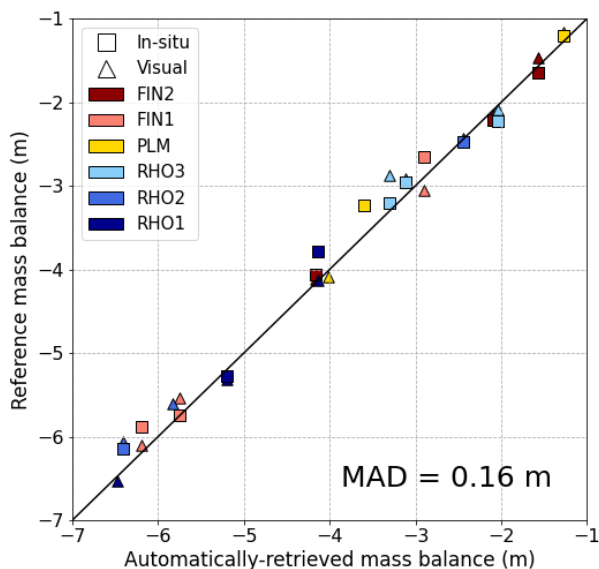


**Figure 7.** Evaluation of the automatically-retrieved cumulative mass balances against the reference mass balance readings, i.e. visual readings and in-situ observations. Results refer to the six stations installed over the summer seasons of 2019–2021. The seasonal mean-absolute deviation (MAD) is 0.16 m.

#### 4.2 Mass balance anomalies and extreme melt events

To detect and assess extreme melt events, the daily observations obtained with the automated method were compared with the long-term average mass balance, yielding daily mass balance anomalies (Fig. 8). According to our definition (cf. Sect. 3.3), an extreme melt event occurs when the anomaly averaged over all the stations exceeds  $-2.55 \text{ cm w.e d}^{-1}$ .

240 In 2019, 11 extreme events were identified (Fig. 8 a). They are distributed more or less evenly over the summer and coincide with high air temperatures, as indicated by meteorological records from MeteoSwiss (Meteoswiss, 2020). In 2020, 14 extreme melt events occurred (Fig. 8 b). Similar to the year 2019, the high-melt days are distributed over the entire summer, although in 2020 more events (ca. 50%) are found in August. In 2021, only three extreme melt events occurred (Fig. 8 c). The year was favourable for the glaciers, with only few days with extreme melting in mid-August and with overall melt close to the decadal  
245 average. This is very much in contrast to 2022, when 23 events of extreme melt occurred (Fig. 8 d). During most of the summer, the anomalies are very negative, exceeding  $-1.5 \text{ cm w.e d}^{-1}$  for a total of 54 days. In addition, various prolonged periods of high melt occurred throughout the summer. The comparison of the four years evidences that the summer of 2022 saw almost as many extreme melt events as the three previous years combined.

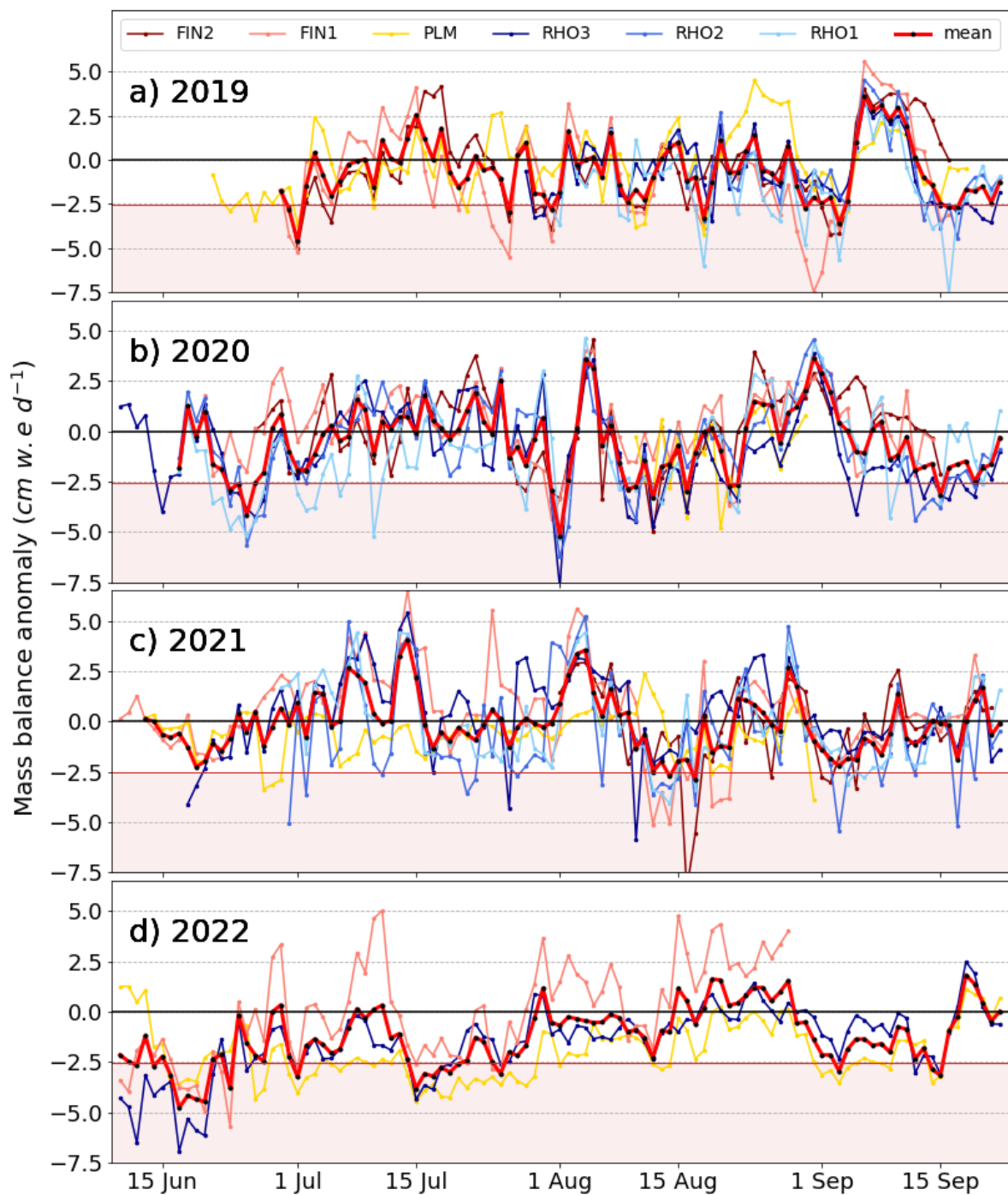


**Figure 8.** Daily mass balance anomalies for the stations on Findelgletscher (reddish colour), Glacier de la Plaine Morte (yellow), and Rhonegletscher (blueish colour) during the summer seasons of (a) 2019, (b) 2020, (c) 2021, and (d) 2022. The mean anomaly for all stations is shown in red (thick line). With our definition (Sect. 3.3), extreme events occur when the mean anomaly exceeds  $-2.55 \text{ cm w. e. d}^{-1}$  (red-shaded area).



### 4.3 Impact of summer 2022 on Swiss-wide glacier storage change

250 To further investigate the influence of extreme melt events and the significance of heat waves on the glacier melt in summer 2022, the daily observations were spatially upscaled to estimate the total storage change of all Swiss glaciers (see Sect. 3.4 for methods). For defining heat waves, we follow Hutter et al. (2007), who defined them as consecutive periods of at least three days during which the mean daily maximum temperature is higher than 30 °C. To have a representative result at the Swiss-wide scale, we considered the average temperature measured at four meteorological stations distributed over Switzerland for defining  
255 heat waves. The four meteorological stations were chosen to be the ones in Lugano (273 m a.s.l.), Chur (556 m a.s.l.), Zurich (426 m a.s.l.), and Sion (482 m a.s.l.). According to this definition, three heat waves occurred during the summer of 2022 for a total of 25 days. The first wave occurred between 17-21 of June, the second between 14-26 of July, and the third between 31 July and 6 August.

Except for August, the Swiss-wide glacier storage change for summer 2022 was significantly higher than the average of  
260 the past decade (Fig. 9). Glacier melt was particularly high during the heat waves in June and July, during which 13 out of 23 extreme melt events occurred. During the August heat wave, instead, melting was not particularly extreme. This is because August melt rates were high during the past decade too, meaning that the melt rate anomalies for August 2022 are not exceeding the threshold we use to define extreme melt events.

In addition to the above, Figure 9 shows ten extreme melt events that occur outside of the heat wave periods. These events  
265 are at the beginning and at the end of the season, i.e. in June and September, when maximal daily air temperatures remain below 30 °C most of the time and thus do not lead to a heat wave in our definition. The temperatures recorded during June and September 2022 were significantly higher than in the past decade and were thus able to cause extreme melt, but were not high enough to be also categorized as heat waves.

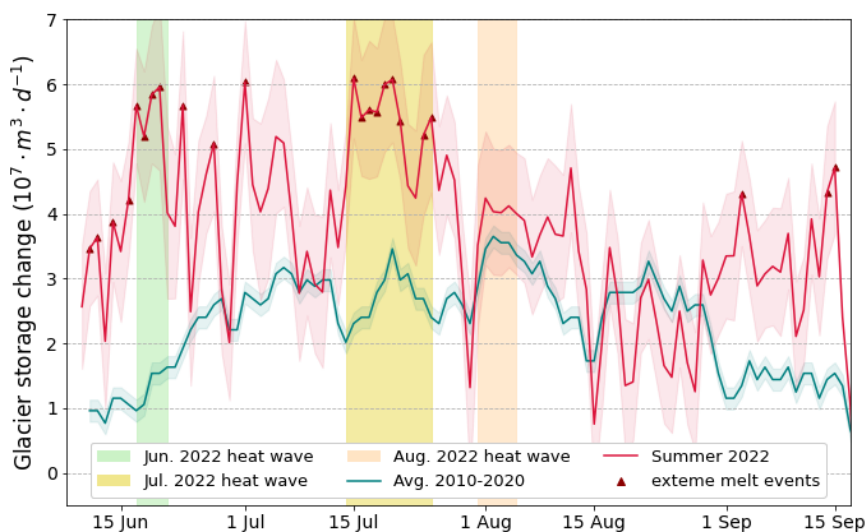


**Figure 9.** Daily storage change of all ca. 1400 Swiss glaciers. The storage change during summer 2022 (red line) is compared to the average storage change of the past decade (blue line). Storage change rates occurring during extreme melt events, defined as days with a mass balance anomaly exceeding  $-2.55 \text{ cm w.e. d}^{-1}$ , are shown by red triangles. The three heat waves that occurred in June, July, and August 2022 are shown in green, yellow, and orange, respectively.

For the period from 10 June to 15 September 2022, we estimate a total storage change for all Swiss glaciers of  $3.63 \pm 0.26 \text{ km}^3 \text{ w.e.}$  (cf. Sect. 5.2 for the uncertainty analysis). This is about 60% more than the average storage change of the past decade during the equivalent period ( $2.25 \pm 0.10 \text{ km}^3 \text{ w.e.}$ ). The annual glacier storage change of 2022 was about three times higher than usual, due to exceptionally low winter accumulation in addition to the high summer ablation (GLAMOS, 2022). During the 25 days of heat waves that occurred in summer 2022, glacier storage change provided  $1.27 \pm 0.10 \text{ km}^3$  of water. This corresponds to 35% of the total glacier storage change of summer 2022, and to 56% of the average summer storage change over the past decade. This demonstrates the significance of extreme melt events occurring during heat waves regarding seasonal glacier melt.

## 5 Discussion

### 5.1 Spatial correlation of point observations

The approach we use for upscaling the mass balance at the regional scale is simple, and we thus investigate the suitability of using point measurements to detect extreme glacier melt events at the regional scale. To do so, we consider the daily mass balance anomalies across stations and compute their correlation for the summer seasons 2019-2021 (Fig. 10). The daily mass balance anomalies correlate well ( $r=0.52-0.82$ , see Fig. 10 a-c) for stations placed on the same glacier, i.e. FIN 1 and FIN 2, as well as RHO 1, RHO 2, and RHO 3. This is in agreement with previous studies showing that glacier mass balance is well correlated over short to intermediate distances (Lliboutry, 1974; Thibert et al., 2013; Vincent et al., 2017, 2018). The correlation





generally decreases between stations that are located on different glaciers. This is expected, since stations on the same glacier  
 285 are more likely to experience the same meteorological forcing. The correlations between the stations on Findelgletscher and  
 Rhonegletscher range from 0.40-0.74, indicating that albeit weaker agreement, the correlation is preserved. The correlations  
 with the station on Glacier de la Plaine Morte, instead, are generally poor. An exception is given by the year 2020, when the  
 correlation is similar to the one between Findelgletscher and Rhonegletscher. This lower correlation was noticed by Landmann  
 et al. (2021) already, who suggested this to be linked to differences in local meteo-climatic conditions (see also discussion  
 290 below).

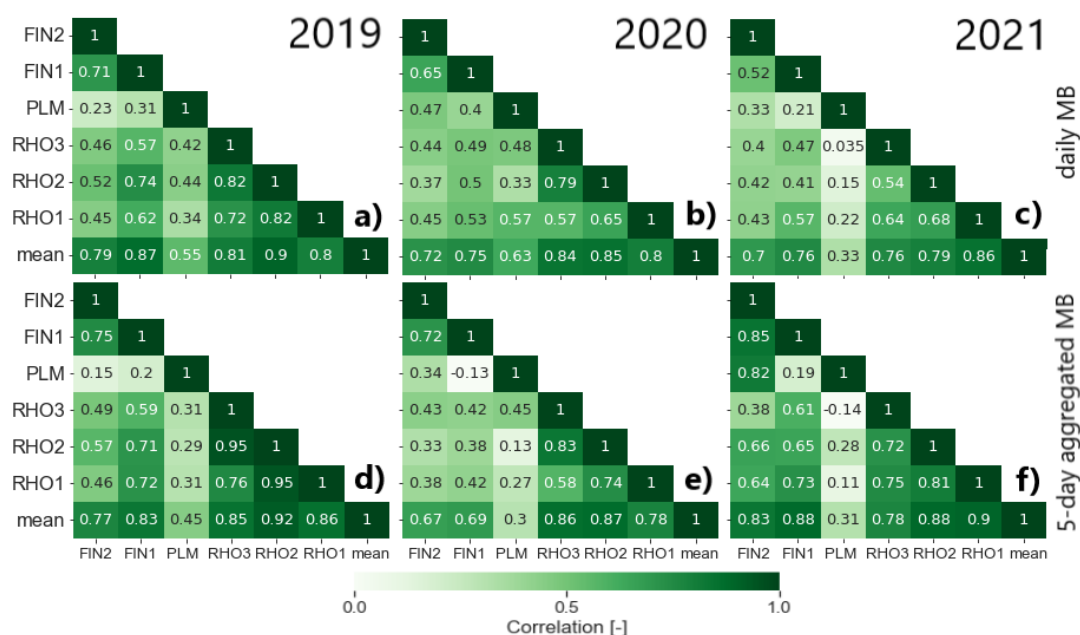


**Figure 10.** Correlation coefficient ( $r$ ) of mass balance anomalies between the different stations. a), b), c) show the correlation of the daily mass balance anomalies between the six stations (indicated by their name) and the correlation between each station and the mean of all stations (labelled "mean"). d), e), and f) show the same, but aggregated over a period of five days.

To investigate whether the uncertainties of the algorithm used to automatically extract the daily mass balances have an influence on the correlation between stations, we aggregate the mass balance anomalies to 5-day periods (Fig. 10 d-f). The argument for doing so is that the uncertainty of the daily readings should be independent from each other, meaning that a reading over a longer period of time should have a smaller relative uncertainty and thus increase the correlation. Indeed, the  
 295 correlations of the so aggregated anomalies increase for stations that are on the same glacier. Similarly, the correlations increase for combinations of stations on Findelgletscher and Rhonegletscher. The anomalies of the stations in Glacier de la Plaine Morte, instead, remain poorly correlated with other stations. The moderate increase in correlation however suggests that the influence of the uncertainties introduced by the automated algorithm are small, thus not affecting our spatial analysis further.



Finally, we computed the correlation between the mean anomaly of all stations and the anomaly at each individual station. This allows assessing whether some stations are more representative than others for the regional-scale signal. The results from both the daily and the 5-days aggregated correlation matrices are congruent (Fig. 10): During the three years with data, the station on Glacier de la Plaine Morte shows a significantly lower correlation with the mean as compared to the other stations. The reason for this is likely to be the different local meteorological forcing: while Findelgletscher and Rhonegletscher are influenced by southerly weather patterns, Glacier de la Plaine Morte experiences weather that is more similar to the Northern flanks of the Alps. This interpretation is corroborated by major differences in winter snow accumulation at the stations: whereas only 1-2 m of snow are typically present in April on the snout of Findel- and Rhonegletscher, more than 4 m are often recorded on Glacier de la Plaine Morte (Bauder et al., 2020; GLAMOS, 2022). Furthermore, the topographical situation of the station on Glacier de la Plaine Morte differs from the other ones: the station is not located at the tongue of a valley glacier, where catabatic winds influence the surface energy balance, but on a glacier plateau surrounded by mountains that might favour cold air trapping. We conclude that the relatively low number of stations and the fact that they are all located in Southwestern Switzerland is limiting when aiming to infer daily mass balance variability at the regional scale, although we note that the stations are located in the region that holds the most glacier area in the Swiss Alps (Linsbauer et al., 2021).

## 5.2 Uncertainty analysis

To estimate the overall uncertainty of the regional mass balance of summer 2022, we account for uncertainties stemming from (A) the automated reading algorithm, (B) the modelled daily mass balance for the period 2010-2020, inferred from seasonal observations at GLAMOS stakes, and (C) the average regional mass balance for the period 2010-2020, used for upscaling.

The uncertainty of the automated reading algorithm ( $\sigma_{alg}$ ) was derived by calculating the mean absolute deviation (MAD) of the automatically-retrieved daily mass balances with respect to the visual readings (Fig. 11 a). The average MAD for the six sites is  $0.81 \text{ cm w.e.d}^{-1}$ . Note that this uncertainty is biased during summer snowfall events due to the large uncertainties of the visual method in such cases. The latter stem from (i) displacements that are very low, and (ii) snow that covers some tapes of the observed stake and the ring at the base of the stake, that serves as reference. This bias is highlighted by the large deviations of the automated readings when visual readings show zero melt (Fig. 11 a). In fact, the algorithm is able to capture smaller displacements than the visual readings, i.e. displacements in the order of a few pixels. Therefore, it appears that the automated method estimates higher ablation for melt rates close to zero, while the visual method fails to capture them. Capturing small displacements also allows measuring melt occurring beneath the fresh snow after summer snowfall events, i.e. when the fresh snow layer is not thick enough to entirely insulate the ice from melt.

Uncertainties of the modelled daily mass balance at the GLAMOS stakes ( $\sigma_b$ ) were derived by conducting a sensitivity analysis (Fig. 11 b). To investigate the model sensitivity to various inputs, the local daily mass balance model was re-run by still ensuring a match with seasonal observations but by varying (i) the meteorological station providing temperature and precipitation forcing, (ii) the gradient to extrapolate air temperature to the site, and (iii) the ratios between the melt factor and radiation factors of the temperature index model (see Huss and Bauder, 2009). The tested range of all variations is large and represents what we would consider a maximum offset from the reference setup, i.e. a conservative estimate for the resulting



uncertainties. The deviation of the mass balance resulting from the different model runs (e.g. varying inputs (i)-(iii)) from the reference mass balance provides the uncertainties  $\sigma_{loc,1}$ ,  $\sigma_{loc,2}$ , and  $\sigma_{loc,3}$ . These uncertainties are considered to be independent  
335 and are combined into an overall uncertainty in local mass balance  $\sigma_b$  for every day as

$$\sigma_b = \sqrt{\sigma_{loc,1}^2 + \sigma_{loc,2}^2 + \sigma_{loc,3}^2}, \quad (8)$$

resulting in daily uncertainties of the modelled point mass balance ranging between 0.19 and 1.18 cm w.e d<sup>-1</sup> (with a mean value of 0.58 cm w.e d<sup>-1</sup>).

Uncertainties in the average regional mass balance for the period 2010-2020 were also estimated based on a sensitivity anal-  
340 ysis (Fig. 11 c). We recomputed the 2010-2020 regional daily glacier mass balance by (i) varying the set of glaciers featuring daily glacier-wide mass balance variations, (ii) randomly superimposing uncertainties in the observation of the glacier-specific ice volume change (Fischer et al., 2015), and (iii) varying the volume-to-mass conversion factor within  $\pm 60 \text{ kg m}^{-3}$ . The deviation of the mass balance resulting from the different model runs (e.g. varying inputs (i)-(iii)) from the reference mass balance provides the uncertainties  $\sigma_{reg,1}$ ,  $\sigma_{reg,2}$ , and  $\sigma_{reg,3}$ . Also here, we combine these uncertainties for every day as

$$\sigma_{\dot{B}_{2010-2020}} = \sqrt{\sigma_{reg,1}^2 + \sigma_{reg,2}^2 + \sigma_{reg,3}^2}. \quad (9)$$

The uncertainty in the daily average mass balance at the scale of all Swiss glaciers  $\sigma_{\dot{B}_{2010-2020}}$  is found to range between 0.06 and 0.21 cm w.e d<sup>-1</sup> (with a mean value of 0.13 cm w.e d<sup>-1</sup>) with highest values during the summer season.

The uncertainty of the regional mass balance of summer 2022 is then derived by combining the uncertainties of (A)  $\sigma_{alg}$ , (B)  $\sigma_b$ , and (C)  $\sigma_{\dot{B}_{2010-2020}}$  as

$$\sigma_{\dot{B}_{2022}} = \sqrt{\sigma_{alg}^2 + \sigma_b^2 + \sigma_{\dot{B}_{2010-2020}}^2}. \quad (10)$$

The mean daily uncertainty of the regional mass balance of summer 2022  $\sigma_{\dot{B}_{2022}}$  is 0.98 cm w.e d<sup>-1</sup>.

Finally, we derive the uncertainty of the Swiss-wide glacier storage change by propagating the uncertainty of the regional mass balance of summer 2022 ( $\sigma_{\dot{B}_{2022}}$ ) and the uncertainty of the Swiss-wide glacier area ( $\sigma_A$ , Linsbauer et al. (2021)) with

$$\sigma_{dS} = dS \cdot \sqrt{\left(\frac{\sigma_A}{A}\right)^2 + \left(\frac{\sigma_{\dot{B}_{2022}}}{\dot{B}_{2022}}\right)^2}. \quad (11)$$

355 The mean daily uncertainty of the Swiss-wide glacier storage change is found to be  $\pm 9.8 \cdot 10^6 \text{ m}^3 \text{ w.e d}^{-1}$ .

Uncertainties of the storage change cumulated over a certain period, i.e. the heat waves and the entire summer, are derived with the same procedure as described in the present section, but first we cumulate the mass balance over the period in question, and then we calculate the corresponding uncertainty assuming all mass balance uncertainties within each period to be independent.

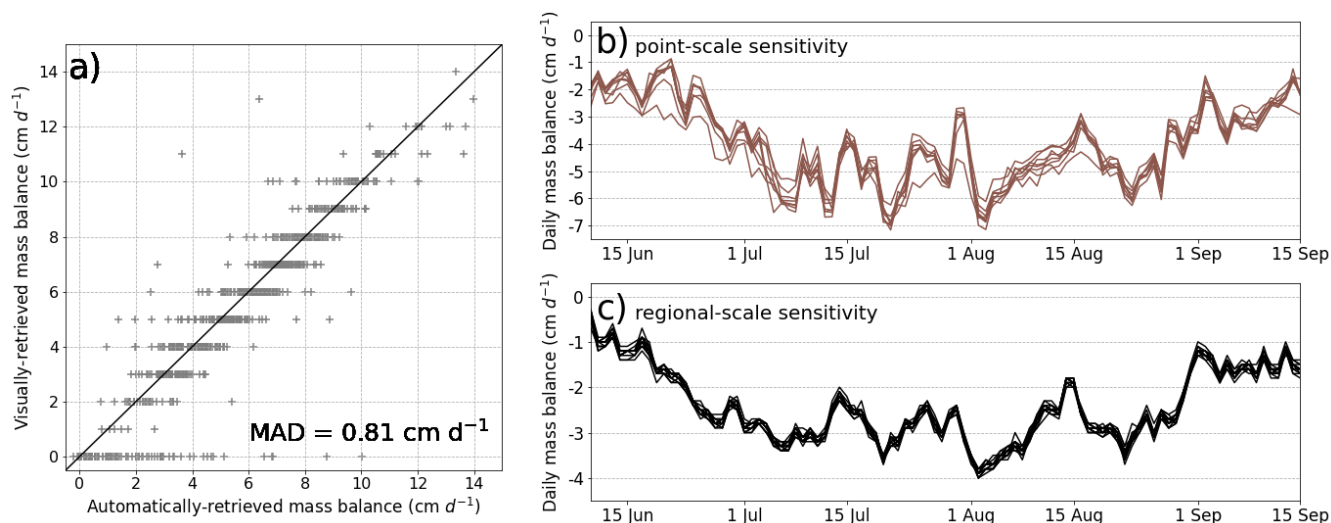


**Figure 11.** Uncertainty assessment. (a) Evaluation of the automated readings against the visual readings. The resolution of the visual readings is  $1 \text{ cm w.e d}^{-1}$ , thus explaining the discrete values on the y-axis. The mean absolute deviation is  $0.81 \text{ cm w.e d}^{-1}$ . (b) Sensitivity analysis of the modelled daily mass balance of the last decade for the GLAMOS stake close to station RHO 3. The point-scale model is run with different setups (individual brown lines) to investigate the sensitivity to various inputs. (c) Sensitivity analysis of the average regional mass balance for the period 2010-2020. Similar to (b), the regional-scale model is run with different setups to investigate its sensitivity.

### 360 5.3 Significance of heat waves

Because glacier melt that occurs during heat waves can be important for mitigating drought conditions (Van Tiel et al., 2021; Ultee et al., 2022), the individual heat waves are compared to each other. The first heat wave occurred in early summer (17-21 June 2022), and glacier melt is categorized as extreme in four out of five days (Fig. 9). The glacier storage change during this heat wave accounts for  $0.30 \pm 0.05 \text{ km}^3 \text{ w.e}$ . Furthermore, the average daily glacier storage change during this  
365 heat wave is  $4.96 \cdot 10^7 \text{ m}^3 \text{ w.e d}^{-1}$ , which is about three times higher than the average daily glacier storage change of the past decade during the equivalent period. The second heat wave occurred between 14-26 July 2022, and glacier melt is categorized as extreme for nine out of thirteen days (Fig. 9). The average daily glacier storage change ( $5.33 \cdot 10^7 \text{ m}^3 \text{ w.e d}^{-1}$ ) is about twice as high as compared to the long-term average, and the total glacier storage change caused by this heat wave is  $0.68 \pm 0.06 \text{ km}^3 \text{ w.e}$ . Even though the average daily glacier storage change has a similar magnitude for the June and the July  
370 heat waves ( $4.96 \cdot 10^7 \text{ m}^3 \text{ w.e d}^{-1}$  and  $5.33 \cdot 10^7 \text{ m}^3 \text{ w.e d}^{-1}$ , respectively), the difference between the daily glacier storage change in 2022 and the decadal average is much higher for the June heat wave. This is because average melt is lower in June, thus making the June heat wave result more anomalous. Nevertheless, the July heat wave was more prolonged, thus causing larger absolute glacier mass loss. The third heat wave occurred between 31 July and 6 August, but during none of the seven days the melt was categorized as extreme (Fig. 9). The average daily glacier storage change, i.e.  $4.05 \cdot 10^7 \text{ m}^3 \text{ w.e d}^{-1}$ , is about  
375 the same as compared to the long-term average, and the amount of water produced during this heat wave is  $0.28 \pm 0.04 \text{ km}^3$ .



The comparison of the three heat waves indicates that the July heat wave was the most severe. This is because of its long duration, causing about the same amount of glacier mass loss as the June and August heat waves combined. In terms of magnitude, instead, the June and July heat waves are similar – the June heat wave being the most intense when compared to the long-term average melt. The comparison also proves the significance of melt occurring during heat waves for determining overall seasonal mass loss, as extreme heat events are expected to increase in the future (Fischer and Schär, 2010; Fischer et al., 2021). Furthermore, the large amounts of water that is produced during such short periods evidences the importance of monitoring short-term glacier mass balance variations. We suggest that this can be particularly important for optimizing the use of glacier runoff for hydropower production, or for an adequate management of water supplies during heat and drought events (Zappa and Kan, 2007; Terrier et al., 2011; Anghileri et al., 2018; Landmann et al., 2021).

## 385 6 Conclusions

In this study, we developed a novel method for the automated derivation of daily glacier mass balance at the point scale. The method is based on computer-vision techniques which are used to read color-taped ablation stakes on time series of close-range camera images. A daily mean absolute deviation of  $0.81 \text{ cm w.e. d}^{-1}$  was found for the automated readings. By comparing the so-derived mass balance time series with the average mass balance of the past decade, we detected extreme melt events in the summer seasons of 2019-2022. A focus was set on summer 2022, which was extraordinary in terms of glacier melt rates. Three severe heat waves were identified, comprising a total of 23 melt events that we classify as extreme. This is about as many events as had occurred over the three previous years, emphasizing the exceptionality of the year. Our approach also detected 25 days of heat wave (i.e. days for which maximum air temperatures averaged over four reference station exceeded  $30^{\circ}\text{C}$ ) during summer 2022, and demonstrated a high correlation between heat waves and extreme melt events. We assessed the glacier storage change that occurred at the scale of Switzerland and found that the 25 days of heat wave occurring during summer 2022 caused an amount of melt that, based on the average over the last decade, is equivalent to 56% of the melt expected for an entire summer. Despite the simplicity of the approach we use to upscale our point observations to the regional mass balance, we showed that extreme melt events occurring during heat days can be determinant for the total seasonal melt.

Our results evidence the importance of real-time observations for studying short-term mass balance variations, and provide a means for improving our understanding of the implications that a future climate – in which more frequent heat waves and extreme melt events are expected – will have on glacier runoff. By emphasizing the large amount of meltwater that is produced during short periods, the study confirms the role that glacier runoff has in attenuating the impacts of heat waves and drought events. We suggest that establishing systems for real-time monitoring of glacier mass balance and runoff could serve to optimize the use of meltwater for hydropower production, as well as to improve the management of water resources in a future, more extreme climate.



*Code and data availability.* The code of the automated algorithm, and the code used to process the data are available online at <https://doi.org/10.5281/zenodo.7405281> (Cremona et al., 2022). Data is currently available at: <https://polybox.ethz.ch/index.php/apps/files/?dir=/Shared&fileid=835395937>. (A DOI will be assigned for the version that will be published)

*Video supplement.* An example application of the automated ice ablation reading for station FIN 1 is available as a video under the following  
410 DOI: <https://doi.org/10.5446/60100> (Cremona, 2022)

*Author contributions.* AC, MH, JML, and DF conceived the study. JB and AC developed the computer vision algorithm, with input from JML and DF. AC processed the images with the algorithm to derive the mass balance for 2019-2022. JML, MH, and AC made the visual readings of the image time series. AC wrote the manuscript and produced the figures, with contributions from all co-authors.

*Competing interests.* At least one of the (co-)authors is a member of the editorial board of The Cryosphere. The peer-review process was  
415 guided by an independent editor, and the authors have no other competing interests to declare.

*Acknowledgements.* This work was conducted in the frame of the project "Machine Learning aided ForecastIng of drought related eXtremes (MaLeFiX)", financed by the program "eXtremes" of the Swiss Federal Institute for Forest, Snow and Landscape Research WSL.



## References

- 420 A2PS contributors: SmartStake: Monitor the glacier ablation with sub-hourly time step and millimetric accuracy, <https://a2photonicsensors.com/smartstake-monitor-glacier-ablation/>, last access on 13 December 2022, 2021.
- Anghileri, D., Botter, M., Castelletti, A., Weigt, H., and Burlando, P.: A comparative assessment of the impact of climate change and energy policies on Alpine hydropower, *Water Resources Research*, 54, 9144–9161, <https://doi.org/10.1029/2017WR022289>, 2018.
- Azam, M., Wagnon, P., Vincent, C., Ramanathan, A., Favier, V., Mandal, A., and Pottakkal, J.: Processes governing the mass balance of  
425 Chhota Shigri Glacier (western Himalaya, India) assessed by point-scale surface energy balance measurements, *The Cryosphere*, 8, 2195–2217, <https://doi.org/10.5194/tc-8-2195-2014>, 2014.
- Bamber, J. L. and Rivera, A.: A review of remote sensing methods for glacier mass balance determination, *Global and Planetary Change*, 59, 138–148, <https://doi.org/10.1016/j.gloplacha.2006.11.031>, 2007.
- Bauder, A., Matthias, H., Linsbauer, A., and (eds.): The Swiss Glaciers 2017/18 and 2018/19: Glaciological Report No. 139/140,  
430 [https://doi.org/10.18752/glrep\\_139-140](https://doi.org/10.18752/glrep_139-140), 2020.
- Bradski, G.: The OpenCV Library, Dr. Dobb's Journal of Software Tools, 2000.
- Braithwaite, R. J.: Positive degree-day factors for ablation on the Greenland ice sheet studied by energy-balance modelling, *Journal of Glaciology*, 41, 153–160, <https://doi.org/10.3189/S0022143000017846>, 1995.
- Carturan, L., Baroni, C., Brunetti, M., Carton, A., Dalla Fontana, G., Salvatore, M. C., Zanoner, T., and Zuecco, G.: Analysis of the mass  
435 balance time series of glaciers in the Italian Alps, *The Cryosphere*, 10, 695–712, <https://doi.org/10.5194/tc-10-695-2016>, 2016.
- Church, J. A., Gregory, J. M., Huybrechts, P., Kuhn, M., Lambeck, K., Nhuan, M. T., Qin, D., and Woodworth, P. L.: Changes in sea level, in: , in: JT Houghton, Y. Ding, DJ Griggs, M. Noguer, PJ Van der Linden, X. Dai, K. Maskell, and CA Johnson (eds.): *Climate Change 2001: The Scientific Basis: Contribution of Working Group I to the Third Assessment Report of the Intergovernmental Panel*, pp. 639–694, Cambridge University Press, 2001.
- 440 Cogley, J. G., Arendt, A., Bauder, A., Braithwaite, R., Hock, R., Jansson, P., Kaser, G., Moller, M., Nicholson, L., Rasmussen, L., et al.: Glossary of glacier mass balance and related terms, *International Hydrological Programme*, 2010.
- Cremona, A.: Example application of the automated ice ablation reading on Findelgletscher, <https://doi.org/10.5446/60100>, 2022.
- Cremona, A., Huss, M., Landmann, J. M., Borner, J., and Farinotti, D.: Heat wave contribution to 2022's extreme glacier melt from automated real-time ice ablation readings [code], <https://doi.org/10.5281/zenodo.7405281>, 2022.
- 445 Cullen, N. J., Mölg, T., Kaser, G., Steffen, K., and Hardy, D. R.: Energy-balance model validation on the top of Kilimanjaro, Tanzania, using eddy covariance data, *Annals of Glaciology*, 46, 227–233, <https://doi.org/10.3189/172756407782871224>, 2007.
- Davaze, L., Rabatel, A., Dufour, A., Hugonnet, R., and Arnaud, Y.: Region-wide annual glacier surface mass balance for the European Alps from 2000 to 2016, *Frontiers in Earth Science*, 8, 149, <https://doi.org/10.3389/feart.2020.00149>, 2020.
- Denzinger, F., Machguth, H., Barandun, M., Berthier, E., Girod, L., Kronenberg, M., Usabaliyev, R., and Hoelzle, M.: Geodetic mass balance  
450 of Abramov Glacier from 1975 to 2015, *Journal of Glaciology*, 67, 331–342, <https://doi.org/10.1017/jog.2020.108>, 2021.
- Dussaillant, I., Berthier, E., and Brun, F.: Geodetic mass balance of the Northern Patagonian Icefield from 2000 to 2012 using two independent methods, *Frontiers in Earth Science*, 6, 8, <https://doi.org/10.3389/feart.2018.00008>, 2018.
- Dyrurgerov, M., Meier, M., and Armstrong, R. L.: *Glacier mass balance and regime: data of measurements and analysis*, vol. 55, Institute of Arctic and Alpine Research, University of Colorado Boulder, 2002.



- 455 Farinotti, D., Pistocchi, A., and Huss, M.: From dwindling ice to headwater lakes: could dams replace glaciers in the European Alps?, *Environmental Research Letters*, 11, 054 022, <https://doi.org/10.1088/1748-9326/11/5/054022>, 2016.
- Fischer, E. M. and Schär, C.: Consistent geographical patterns of changes in high-impact European heatwaves, *Nature Geoscience*, 3, 398–403, <https://doi.org/10.1038/ngeo866>, 2010.
- Fischer, E. M., Sippel, S., and Knutti, R.: Increasing probability of record-shattering climate extremes, *Nature Climate Change*, 11, 689–695, <https://doi.org/10.1038/s41558-021-01092-9>, 2021.
- 460 Fischer, M., Huss, M., and Hoelzle, M.: Surface elevation and mass changes of all Swiss glaciers 1980–2010, *The Cryosphere*, 9, 525–540, <https://doi.org/10.5194/tc-9-525-2015>, 2015.
- Fitzpatrick, N., Radić, V., and Menounos, B.: Surface energy balance closure and turbulent flux parameterization on a mid-latitude mountain glacier, Purcell Mountains, Canada, *Frontiers in Earth Science*, 5, 67, <https://doi.org/10.3389/feart.2017.00067>, 2017.
- 465 Fountain, A. G. and Vecchia, A.: How many stakes are required to measure the mass balance of a glacier?, *Geografiska Annaler: Series A, Physical Geography*, 81, 563–573, <https://doi.org/10.1111/1468-0459.00084>, 1999.
- Friederichs, P.: Statistical downscaling of extreme precipitation events using extreme value theory, *Extremes*, 13, 109–132, <https://doi.org/10.1007/s10687-010-0107-5>, 2010.
- Friederichs, P., Wahl, S., and Buschow, S.: Postprocessing for extreme events, in: *Statistical Postprocessing of Ensemble Forecasts*, pp. 127–154, Elsevier, <https://doi.org/10.1016/B978-0-12-812372-0.00005-4>, 2018.
- 470 Geibel, L., Huss, M., Kurzböck, C., Hodel, E., Bauder, A., and Farinotti, D.: Rescue and homogenization of 140 years of glacier mass balance data in Switzerland, *Earth System Science Data*, 14, 3293–3312, <https://doi.org/10.5194/essd-14-3293-2022>, 2022.
- GLAMOS: Swiss Glacier Mass Balance, release 2021, *Glacier Monitoring Switzerland*, <https://doi.org/10.18750/massbalance.2020.r2021>, 2021.
- 475 GLAMOS: Swiss Glacier Mass Balance, release 2022, *Glacier Monitoring Switzerland*, <https://doi.org/10.18750/massbalance.2022.r2022>, 2022.
- Grab, M., Mattea, E., Bauder, A., Huss, M., Rabenstein, L., Hodel, E., Linsbauer, A., Langhammer, L., Schmid, L., Church, G., Hellmann, S., Déléze, K., Schaer, P., Lathion, P., Farinotti, D., and Maurer, H.: Ice thickness distribution of all Swiss glaciers based on extended ground-penetrating radar data and glaciological modeling, *Journal of Glaciology*, 67, 1074–1092, <https://doi.org/10.1017/jog.2021.55>, 2021.
- 480 Gugerli, R., Salzmann, N., Huss, M., and Desilets, D.: Continuous and autonomous snow water equivalent measurements by a cosmic ray sensor on an alpine glacier, *The Cryosphere*, 13, 3413–3434, <https://doi.org/10.5194/tc-13-3413-2019>, 2019.
- Hock, R.: Glacier melt: a review of processes and their modelling, *Progress in Physical Geography*, 29, 362–391, <https://doi.org/10.1191/0309133305pp453ra>, 2005.
- 485 Hock, R., Bliss, A., Marzeion, B., Giesen, R. H., Hirabayashi, Y., Huss, M., Radić, V., and Slangen, A. B.: GlacierMIP—A model intercomparison of global-scale glacier mass-balance models and projections, *Journal of Glaciology*, 65, 453–467, <https://doi.org/10.1017/jog.2019.22>, 2019.
- Hugonnet, R., McNabb, R., Berthier, E., Menounos, B., Nuth, C., Girod, L., Farinotti, D., Huss, M., Dussailant, I., Brun, F., et al.: Accelerated global glacier mass loss in the early twenty-first century, *Nature*, 592, 726–731, <https://doi.org/10.1038/s41586-021-03436-z>, 2021.
- 490 Huss, M.: Extrapolating glacier mass balance to the mountain-range scale: the European Alps 1900–2100, *The Cryosphere*, 6, 713–727, <https://doi.org/10.5194/tc-6-713-2012>, 2012.





- Huss, M.: Density assumptions for converting geodetic glacier volume change to mass change, *The Cryosphere*, 7, 877–887, <https://doi.org/10.5194/tc-7-877-2013>, 2013.
- Huss, M. and Bauder, A.: 20th-century climate change inferred from four long-term point observations of seasonal mass balance, *Annals of Glaciology*, 50, 207–214, <https://doi.org/10.3189/172756409787769645>, 2009.
- 495 Huss, M. and Hock, R.: Global-scale hydrological response to future glacier mass loss, *Nature Climate Change*, 8, 135–140, <https://doi.org/10.1038/s41558-017-0049-x>, 2018.
- Huss, M., Bauder, A., Linsbauer, A., Gabbi, J., Kappenberger, G., Steinegger, U., and Farinotti, D.: More than a century of direct glacier mass-balance observations on Claridenfirn, Switzerland, *Journal of Glaciology*, 67, 697–713, <https://doi.org/10.1017/jog.2021.22>, 2021.
- 500 Hutter, H.-P., Moshhammer, H., Wallner, P., Leitner, B., and Kundi, M.: Heatwaves in Vienna: effects on mortality, *Wiener Klinische Wochenschrift*, 119, 223–227, <https://doi.org/10.1007/s00508-006-0742-7>, 2007.
- Immerzeel, W. W., Van Beek, L. P., and Bierkens, M. F.: Climate change will affect the Asian water towers, *Science*, 328, 1382–1385, <https://doi.org/10.1126/science.1183188>, 2010.
- Immerzeel, W. W., Lutz, A., Andrade, M., Bahl, A., Biemans, H., Bolch, T., Hyde, S., Brumby, S., Davies, B., Elmore, A., et al.: Importance and vulnerability of the world’s water towers, *Nature*, 577, 364–369, <https://doi.org/10.1038/s41586-019-1822-y>, 2020.
- 505 Landmann, J. M., Künsch, H. R., Huss, M., Ogier, C., Kalisch, M., and Farinotti, D.: Assimilating near-real-time mass balance stake readings into a model ensemble using a particle filter, *The Cryosphere*, 15, 5017–5040, <https://doi.org/10.5194/tc-15-5017-2021>, 2021.
- Linsbauer, A., Huss, M., Hodel, E., Bauder, A., Fischer, M., Weidmann, Y., Bärtschi, H., and Schmassmann, E.: The New Swiss Glacier Inventory SGI2016: from a topographical to a glaciological dataset, *Frontiers in Earth Science*, 9, 774, <https://doi.org/10.3389/feart.2021.704189>, 2021.
- 510 Liboutry, L.: Multivariate Statistical Analysis of Glacier Annual Balances, *Journal of Glaciology*, 13, 371–392, <https://doi.org/10.3189/S0022143000023169>, 1974.
- Marzeion, B., Hock, R., Anderson, B., Bliss, A., Champollion, N., Fujita, K., Huss, M., Immerzeel, W. W., Kraaijenbrink, P., Malles, J.-H., et al.: Partitioning the uncertainty of ensemble projections of global glacier mass change, *Earth’s Future*, 8, e2019EF001470, <https://doi.org/10.1029/2019EF001470>, 2020.
- 515 Meteoswiss: Klimabulletin Jahr 2019, Tech. rep., Federal Office of Meteorology and Climatology, MeteoSwiss, 2020.
- Mölg, N., Ceballos, J. L., Huggel, C., Micheletti, N., Rabatel, A., and Zemp, M.: Ten years of monthly mass balance of Conejeras glacier, Colombia, and their evaluation using different interpolation methods, *Geografiska Annaler: Series A, Physical Geography*, 99, 155–176, <https://doi.org/10.1080/04353676.2017.1297678>, 2017.
- 520 Ohmura, A., Bauder, A., Müller, H., and Kappenberger, G.: Long-term change of mass balance and the role of radiation, *Annals of Glaciology*, 46, 367–374, <https://doi.org/10.3189/172756407782871297>, 2007.
- O’Neel, S., McNeil, C., Sass, L. C., Florentine, C., Baker, E. H., Peitzsch, E., McGrath, D., Fountain, A. G., and Fagre, D.: Reanalysis of the US Geological Survey Benchmark Glaciers: long-term insight into climate forcing of glacier mass balance, *Journal of Glaciology*, 65, 850–866, <https://doi.org/10.1017/jog.2019.66>, 2019.
- 525 OpenCV: OpenCV: template matching, [https://docs.opencv.org/master/d4/dc6/tutorial\\_py\\_template\\_matching.html](https://docs.opencv.org/master/d4/dc6/tutorial_py_template_matching.html), last access on 20 October 2020, 2022.
- Ostrem, G. and Stanley, A.: Glacier mass-balance measurements – A manual for field and office work, Department of Energy, Mines and Resources, Ottawa, Ontario; Norwegian Water Resources and Electricity Board, Oslo, 1969.



- 530 Parkes, D. and Marzeion, B.: Twentieth-century contribution to sea-level rise from uncharted glaciers, *Nature*, 563, 551–554, <https://doi.org/10.1038/s41586-018-0687-9>, 2018.
- Patro, E. R., De Michele, C., and Avanzi, F.: Future perspectives of run-of-the-river hydropower and the impact of glaciers' shrinkage: The case of Italian Alps, *Applied Energy*, 231, 699–713, <https://doi.org/10.1016/j.apenergy.2018.09.063>, 2018.
- Pellicciotti, F., Brock, B., Strasser, U., Burlando, P., Funk, M., and Corripio, J.: An enhanced temperature-index glacier melt model including the shortwave radiation balance: development and testing for Haut Glacier d'Arolla, Switzerland, *Journal of Glaciology*, 51, 573–587, <https://doi.org/10.3189/172756505781829124>, 2005.
- Schaepli, B., Manso, P., Fischer, M., Huss, M., and Farinotti, D.: The role of glacier retreat for Swiss hydropower production, *Renewable Energy*, 132, 615–627, <https://doi.org/10.1016/j.renene.2018.07.104>, 2019.
- Sold, L., Huss, M., Machguth, H., Joerg, P. C., Leysinger Vieli, G., Linsbauer, A., Salzmann, N., Zemp, M., and Hoelzle, M.: Mass balance re-analysis of Findelengletscher, Switzerland; benefits of extensive snow accumulation measurements, *Frontiers in Earth Science*, 4, 18, <https://doi.org/10.3389/feart.2016.00018>, 2016.
- 540 Stoffel, M. and Huggel, C.: Effects of climate change on mass movements in mountain environments, *Progress in Physical Geography*, 36, 421–439, <https://doi.org/10.1177/0309133312441010>, 2012.
- Terrier, S., Jordan, F., Schleiss, A., Haerberli, W., Huggel, C., and Künzler, M.: Optimized and adapted hydropower management considering glacier shrinkage scenarios in the Swiss Alps, in: *Proc. of International Symposium on Dams and Reservoirs under Changing Challenges, 79th Annual Meeting of ICOLD – Swiss Committee on Dams*, pp. 497–508, CRC Press, Taylor & Francis Group, 2011.
- 545 Thibert, E., Eckert, N., and Vincent, C.: Climatic drivers of seasonal glacier mass balances: an analysis of 6 decades at Glacier de Sarennes (French Alps), *The Cryosphere*, 7, 47–66, <https://doi.org/10.5194/tc-7-47-2013>, 2013.
- Thibert, E., Dkengne Sielenou, P., Vionnet, V., Eckert, N., and Vincent, C.: Causes of glacier melt extremes in the Alps since 1949, *Geophysical Research Letters*, 45, 817–825, <https://doi.org/10.1002/2017GL076333>, 2018.
- 550 Trewin, B., Cazenave, A., Howell, S., Huss, M., Isensee, K., Palmer, M. D., Tarasova, O., and Vermeulen, A.: Headline indicators for global climate monitoring, *Bulletin of the American Meteorological Society*, 102, E20–E37, <https://doi.org/10.1175/BAMS-D-19-0196.1>, 2021.
- Ultee, L., Coats, S., and Mackay, J.: Glacial runoff buffers droughts through the 21st century, *Earth System Dynamics*, 13, 935–959, <https://doi.org/10.5194/esd-13-935-2022>, 2022.
- Van Tiel, M., Van Loon, A. F., Seibert, J., and Stahl, K.: Hydrological response to warm and dry weather: do glaciers compensate?, *Hydrology and Earth System Sciences*, 25, 3245–3265, <https://doi.org/10.5194/hess-25-3245-2021>, 2021.
- 555 Vincent, C., Fischer, A., Mayer, C., Bauder, A., Galos, S. P., Funk, M., Thibert, E., Six, D., Braun, L., and Huss, M.: Common climatic signal from glaciers in the European Alps over the last 50 years, *Geophysical Research Letters*, 44, 1376–1383, <https://doi.org/10.1002/2016GL072094>, 2017.
- Vincent, C., Soruco, A., Azam, M., Basantes-Serrano, R., Jackson, M., Kjølmoen, B., Thibert, E., Wagnon, P., Six, D., Rabatel, A., et al.: A nonlinear statistical model for extracting a climatic signal from glacier mass balance measurements, *Journal of Geophysical Research: Earth Surface*, 123, 2228–2242, <https://doi.org/10.1029/2018JF004702>, 2018.
- 560 Zappa, M. and Kan, C.: Extreme heat and runoff extremes in the Swiss Alps, *Natural Hazards and Earth System Sciences*, 7, 375–389, <https://doi.org/10.5194/nhess-7-375-2007>, 2007.
- Zemp, M., Hoelzle, M., and Haerberli, W.: Six decades of glacier mass-balance observations: a review of the worldwide monitoring network, *Annals of Glaciology*, 50, 101–111, <https://doi.org/10.3189/172756409787769591>, 2009.
- 565



- Zemp, M., Thibert, E., Huss, M., Stumm, D., Rolstad Denby, C., Nuth, C., Nussbaumer, S. U., Moholdt, G., Mercer, A., Mayer, C., et al.: Reanalysing glacier mass balance measurement series, *The Cryosphere*, 7, 1227–1245, <https://doi.org/10.5194/tc-7-1227-2013>, 2013.
- Zemp, M., Frey, H., Gärtner-Roer, I., Nussbaumer, S. U., Hoelzle, M., Paul, F., Haeberli, W., Denzinger, F., Ahlstrøm, A. P., Anderson, B., et al.: Historically unprecedented global glacier decline in the early 21st century, *Journal of Glaciology*, 61, 745–762, <https://doi.org/10.3189/2015JoG15J017>, 2015.
- 570 Zemp, M., Huss, M., Thibert, E., Eckert, N., McNabb, R., Huber, J., Barandun, M., Machguth, H., Nussbaumer, S. U., Gärtner-Roer, I., et al.: Global glacier mass changes and their contributions to sea-level rise from 1961 to 2016, *Nature*, 568, 382–386, <https://doi.org/10.1038/s41586-019-1071-0>, 2019.